ABSTRACT

The influence of synthetic conditions in the composition and properties of chemically precipitated hydroxyapatite (HAp), fluorine-substituted HAp (*x*F-HAp) and fluorapatite (FAp) have been examined considering different atmospheres (nitrogen, air and carbon dioxide), temperatures (37 ºC and 150 ºC) and pressures (hydrothermal conditions). Results indicate that the synthetic conditions not only affect the fluorination degree but also have a pronounced effect on the carbonation degree, the crystallinity, the surface wettability and the thermal stability. Besides, the electrical polarization of HAp-based minerals mainly depends on the fluoride content, the formation of ordered channels of vacancies along the sintering and thermal polarization processes becoming more difficult with increasing fluorination degree. This limits the utilization of *x*F-HAp and FAp as electro-responsive scaffolds and electrocatalysts, as has been recently proposed for polarized HAp. Finally, the effects of the carbonation and the fluoridation degrees, the concentration fluoride anions supplied from an external source, and the pH on the solubility of HAp-based minerals have been examined. Observations indicate that, although strategies based on the substitution of HAp by *x*F-HAp or FAp have been proposed for coatings of dental implants, external fluoride anions inhibit the solubility more effectively than the fluorination of the own mineral matrix. Accordingly, HAp combined with an effective external supply of fluoride anions is more appropriated than *x*F-HAp and FAp for the fabrication of dental coatings.

Keywords: Carbonation; Chemical precipitation; Crystallinity; Fluorapatite; Fluorination degree

INTRODUCTION

Fluorapatite (FAp), $Ca_{10}(PO_4)_6F_2$, is the most stable, least soluble and hardest calcium orthophosphate mineral [1-3]. Compared to hydroxyapatite (HAp), $Ca_{10}(PO_4)_6(OH)_2$, FAp is prepared using similar synthetic procedures but introducing CaF, NaF or NH_4F to transmit fluoride (F^-) ions [4]. Moreover, previous studies have suggested that FAp and HAp exhibit similar biocompatibility in terms of fixation to bone and bone in-growth [5-7]. Indeed, among all human calcified tissues, the greatest concentration of FAp is found in bones, and the lowest in enamel [8]. However, even where there is the largest concentration of FAp, the amount of F^- is usually reduced to stoichiometric quantities.

FAp has been mainly used as clinical restorative material [9,10] and as a catalyst [11,12]. Regarding to the former application and considering that the ionic substitution (doping) of HAp is a relatively easy process [13-17], in the last decade fluorine-substituted HAp has attracted substantial attention [18-24] because F^- ions can reduce the formation of caries in bacterially contaminated environments and promotes mineralization and crystallization of calcium phosphates in the formation of bone [25]. In spite of the physiological significance of F^- ions, the utilization of FAp and, in general, of fluorine-substituted HAp as clinical restoration materials is limited due to their very low solubility, since they exhibit much lower bioresorption rate than HAp [2].

On the other hand, carbonate (CO_3^{2-}) is also present in biological apatites (enamel, dentine, bone, and pathological calcifications) by substitution at phosphate (PO_4^{3-}) and hydroxide (OH^-) sites, tending to increase its solubility in comparison with pure HAp [26-27]. Indeed, CO_3^{2-} substitution has been recently used to enhance the HAp solubility and to promote other desired properties (*e.g.* the antibacterial effect in silver-substituted HAp [28], the bioresorption capacity [29], and the ionic substitution [30]).

In this work, we combine the impact of the simultaneous incorporation of F^-or/and CO_3^{2-} ions in the properties of HAp. For this purpose, fluorine-substituted minerals with different fluorination and carbonation degrees have been prepared by controlling the atmosphere and temperature during the chemical precipitation process. After this, the influence of the composition on the spectroscopic, structural, thermal, solvent-affinity (wettability and water absorption) and electrochemical properties of the resulting minerals has been evaluated. Finally, the impact of the carbonation and fluorination degrees of the HAp matrix, the concentration of externally supplied F^- anions, and the pH on the solubility of HAp have been examined. Results are in controversy with recent recommendations for the fabrication of mineral coatings for dental implants according which it was proposed to replace HAp by fluorine-substituted HAp.

METHODS

Synthesis

Hydroxyapatite (HAp). The reagent conditions used to prepare HAp were adjusted to get a Ca/P ratio of 1.67. In all cases 15 mL of 0.5 M $(NH_4)_2HPO_4$ in de-ionized water (pH adjusted to 11 with an ammonia 30% w/w solution) were added drop-wise (rate of 2 $mL \cdot min^{-1}$) and under agitation (400 rpm) to 25 mL of 0.5 M $Ca(NO_3)_2$ in ethanol. After that, the reaction mixture was stirred (400 rpm) for 1 hour at room temperature. Resultant suspension was aged for 48 h at 37 ºC. The precipitate was separated by centrifugation and washed sequentially with de-ionized water and a 60/40 v/v mixture of ethanol-water (twice). A white powder was obtained after freeze-drying. Particles were filtered through a 0.22 μm filter (Millipore, Billerica, MA). Filtration was performed at a flow rate of 1 mL/min using a 10 mL syringe and concentration of the

particles was achieved using an IE C MultiRF centrifugue (Thrrmo IEC, Needham Heights, MA, USA).

Fluorine substituted HAp (xF-HAp) and fluorapatite (FAp). Solid solutions with formula $Ca_{10}(PO_4)_6(OH)_{2-x}F_x$ were obtained by incorporating F^- instead of OH^- groups. In all cases 0.5 M NH_4F was added into a constantly stirred Ca and P containing solution, prepared as described above. Different amounts (from 1 mL for 0.4F-HAp to 5 mL for FAp) of 0.5 M ammonia fluoride solution were added individually to control the value *x* in the general formula. When *x* was 0 and 1 the obtained powders were named HAp and FAp, respectively, while the ceramic compositions with *x*= 0.4, 0.8, 1.2 and 1.6 were denoted 0.4F-HAp, 0.8F-HAp, 1.2F-HAp and 1.6F-HAp, respectively (*x* refers to the degree of fluorination).

Three different experimental conditions were considered for the precipitation:

- Atmospheric (ATM) conditions. The precipitation mixture was stirred 1 hour by agitation (400 rpm) at 37 ºC or 150 ºC under atmospheric conditions, hereafter denoted ATM(37ºC)- and ATM(150ºC)-conditions, respectively. It is worth nothing that ATM(37ºC)-conditions correspond to those used for the preparation of HAp (see above).

- Hydrothermal (HT) conditions. The reaction mixture was stirred 24 hours by agitation (400 rpm) at 150 ºC under a pressure of 20 bars.

- Nitrogen (N_2) conditions. The precipitation occurred after stirring (400 rpm) for 1 hour at 37 ºC or 150 ºC under inert N_2 atmosphere, hereafter denoted N_2(37ºC)- and N_2(150ºC)-conditions, respectively.

- Carbon dioxide (CO_2) conditions. The precipitation occurred after stirring (400 rpm) during an interval comprised between 1 and 3 hours, depending on the desired

CO_3^{2-} content, at 37 ºC under CO_2 atmosphere. Thus, these conditions have been employed to regulate the carbonation degree of *x*F-HAp and FAp.

Discs preparation. HAp, *x*F-HAp and FAp powders were uniaxially pressed at 620 MPa for 10 min to obtain dense discs suitable for characterization. The dimensions of these specimens were 10 mm of diameter × 1.7 mm of thickness.

Characterization

FTIR spectroscopy. Infrared absorption spectra were recorded with a Fourier Transform FTIR 4100 Jasco spectrometer in the 1800-700 cm^{-1} range. A Specac model MKII Golden Gate attenuated total reflection (ATR) equipment with a heated Diamond ATR Top-Plate was used.

X-ray photoelectron spectroscopy (XPS). XPS analyses were performed in a SPECS system equipped with a high-intensity twin-anode X-ray source XR50 of Mg/Al (1253 eV/1487 eV) operating at 150 W, placed perpendicular to the analyzer axis, and using a Phoibos 150 MCD-9 XP detector. The X-ray spot size was 650 µm. The pass energy was set to 25 and 0.1 eV for the survey and the narrow scans, respectively. Charge compensation was achieved with a combination of electron and argon ion flood guns. The energy and emission current of the electrons were 4 eV and 0.35 mA, respectively. For the argon gun, the energy and the emission current were 0 eV and 0.1 mA, respectively. The spectra were recorded with pass energy of 25 eV in 0.1 eV steps at a pressure below 6×10^{-9} mbar. These standard conditions of charge compensation resulted in a negative but perfectly uniform static charge. The C 1s peak was used as an internal reference with a binding energy of 284.8 eV. High-resolution XPS spectra were acquired by Gaussian–Lorentzian curve fitting after s-shape background subtraction. The surface composition was determined using the manufacturer's sensitivity factors.

X-Ray diffraction. Crystallinity was studied by wide angle X-ray diffraction (WAXD). Patterns were acquired using a Bruker D8 Advance model with Cu K_α radiation (λ = 0.1542 nm) and geometry of Bragg-Bretano, θ–2θ. A one-dimensional Lynx Eye detector was employed. Samples were run at 40 kV and 40 mA, with a 2θ range of 10º-60º, measurement steps of 0.02º, and time/step of 2-8 s. Diffraction profiles were processed using PeakFit v4 software (Jandel Scientific Software) and the graphical representation performed with OriginPro v8 software (OriginLab Corporation, USA).

The crystallite size (L) of HAp, xF-HAp and FAp samples was determined in the direction perpendicular to the (211) planes from the X-ray diffraction line broadening measurement using the Scherrer equation:

$$L = \frac{0.9\lambda}{\beta \cos\theta} \qquad (1)$$

where λ is the wavelength (CuK_α), β is the full width at half maximum height of the (211) line, θ is the diffraction angle and 0.9 is a shape factor.

The crystallinity (χ_c) was obtained using the following Eqn:

$$\chi_c = 1 - \frac{V_{112/300}}{I_{300}} \qquad (2)$$

where I_{300} is the intensity of the (300) reflection and $V_{112/300}$ is the intensity of the hollow between the (112) and (300) reflections, which disappears in non-crystalline samples.

Thermal stability Thermogravimetric analyses (TGA) for studying thermal stability at relatively low temperatures (< 600 ºC) were performed at a heating rate of 20 ºC/min (sample weight *ca.* 5 mg) with a Q50 thermogravimetric analyser of TA Instruments and under a flow of dry nitrogen. Test temperatures ranged from 30 to 600 ºC.

Wettability. Contact angle measurements for water and fetal bovine serum (FBS), a growth supplement for cell culture media, were carried out using the sessile drop

method. Images of milliQ water drops (0.5 μL) were recorded after stabilization with the equipment OCA 15EC (Data-Physics Instruments GmbH, Filderstadt). SCA20 software was used to analyze the images and determine the contact angle value, which was obtained as the average of at least ten independent measures for each sample.

Water absorption. The water absorption capacity (WA, %) of mineral discs was determined according to:

$$WA = \frac{w_W - w_D}{w_D} \quad (3)$$

where w_W is the weight of the discs after being immersed in milli-Q water for 60 min and w_D is the weight of the discs dried at room temperature.

Cyclic voltammetry (CV). The electrochemical behavior of the prepared mineral was determined by CV using an Autolab PGSTAT302N equipped with the ECD module (Ecochimie, The Netherlands) using a three-electrode cell. Experiments were conducted under a nitrogen atmosphere (99.995% in purity) at room temperature. A 0.1 M phosphate buffer saline solution (PBS; pH= 7.2 adjusted with NaOH) was used as the electrolyte in the three-electrode cell. The working compartment was filled with 30 mL of the electrolyte solution. Steel AISI 316 sheets of 1×1.5 cm^2 (thickness 0.1 cm) were used as both the working and the counter electrodes, and an Ag|AgCl electrode was used as the reference electrode which contained a KCl saturated aqueous solution (offset potential versus the standard hydrogen electrode, E^0 = 0.222 V at 25 °C). All potentials given in this work are referenced to this electrode. HAp, *x*F-HAp and FAp discs prepared as described above were fixed on the working electrode using a two-side adhesive carbon layer. The initial and final potentials were -0.40 V, whereas a reversal potential of 0.80 V was considered. The scan rate was 50 mV/s. The electroactivity, which indicates the ability to exchange charge reversibly, was evaluated by examining

the similarity between the anodic and cathodic areas of the control voltammogram (*i.e.* the ratio between the reduction and oxidation charges).

Solubility. The mass solubility of HAp, *x*F-HAp and FAp was determined by gravimetry in a solution of de-ionized water with 100 mM HCl and 50 mM NaCl at room temperature and atmospheric pressure. More specifically, 500 mg of pulverized solid mineral were added to 50 mL of solution, and agitated by a magnetic stirrer overnight. After this time, the oversaturated solution was filtered and the residue was dried in a lyophilizer during 72 h. The masses were determined using a CPA26P Sartorius analytical microbalance with a precision of $2 \cdot 10^{-6}$ g.

RESULTS AND DISCUSSION

Spectroscopic characterization

The FTIR spectra of HAp, *x*F-HAp and FAp prepared using ATM(37ºC)- and N_2(37ºC)-conditions show typical PO_4^{3-} bands at the region comprised between 950 and 1200 cm^{-1} (Figure 1): $\nu_1 \approx 955$ cm^{-1} and $\nu_3 = 1016, 1084$ cm^{-1} [31]. However, comparison of the spectra indicate that the atmosphere used during the precipitation process significantly affects the composition of the samples. Thus, samples prepared under ATM(37ºC)-conditions show absorption bands at 3242 and 3033 cm^{-1}, which are associated to the adsorbed water, and at 820 cm^{-1} (ν_2) and 1416, 1308 cm^{-1} (ν_3) due to CO_3^{2-}. The position of these bands is consistent with the predominant B-type substitution, according to which PO_4^{3-} is replaced by CO_3^{2-} (*i.e.* the bands of A-type CO_3^{2-}, which replace OH^-, usually appear at higher wavenumbers) [32]. Moreover, the intensity of the CO_3^{2-} bands increases significantly with the F^- intake, while it is negligible for HAp. This feature suggests that HAp fluoridation in non-controlled

ATM-conditions promotes the substitution of PO_4^{3-} by CO_3^{2-}. In opposition, the intensity of water and CO_3^{2-} absorption bands is imperceptible for *x*F-HAp and FAp samples obtained under N_2-conditions (Figure 1b).

Although the FTIR spectra of samples prepared using ATM(150ºC)- and N_2(150ºC)-conditions are similar to those described above (Figure S1), they exhibit some differential features. The most remarkable one is that the absorption of water in samples prepared under ATM(150ºC)-conditions decreases drastically with respect to those obtained using ATM(37ºC)-conditions (Figure S1a). Also, the CO_3^{2-} bands become less intense at the highest temperature, even though they occur at the same positions confirming the predominant B-type substitution. Moreover, the intensity of the CO_3^{2-} increases with the F^- content, which is consistent with the boosting effect of fluoridation in the PO_4^{3-} by CO_3^{2-} discussed above. On the other hand, the protective effect exerted by the N_2 atmosphere with respect to the adsorption of water and the incorporation of CO_3^{2-} is preserved at 150 ºC (Figure S1b).

The presence of F^- in *x*F-HAp and FAp samples prepared under ATM(37ºC)-conditions is demonstrated in Figure 1c. High resolution XPS spectra in the F 1s region of *x*F-HAp show a peak located at 684.1 eV, which is the fingerprint that proves that F^- ions have been successfully incorporated into the lattice HAp structure [33]. Interestingly, for FAp the XPS spectrum in the F 1s region presents two peaks. In this case, the second peak, which is centered at 686.5 eV, has been associated to the formation of CaF_2 traces when the concentration of F^- ions coming from the addition of NH_4F to the reaction solution is the maximum [34].

Table 1 compares the atomic percent compositions of HAp, *x*F-HAp and FAp samples prepared under N_2(37ºC)-conditions. As it can be seen, the Ca/P ratio increases

from 1.60 (HAp) to 1.67 with the fluorine content. This feature has been related with the influence of F^- and OH^- sizes (F^- < OH^-) in the reaction kinetics. Thus, the incorporation of small F^- anions is faster than that of OH^- anions producing the expected Ca/P ratio of 1.67 only when the degree of fluorination is the maximum (x= 2). When x < 2, the fluoride content is not enough to complete the reaction, inducing the deficiency of calcium (Ca/P < 1.67). The maximum deficiency is reached when the fluoride content is null (HAp). The increment of the F/Ca ratio accompanies the one of the Ca/P ratio, proving that the incorporation of F^- increases with the amount of NH_4F solution added to the reaction medium. The maximum value reached for the F/Ca ratio was 0.190, which is still below the stoichiometric limit of FAp, *i.e.* F/Ca= 2/10= 0.200 for $Ca_{10}(PO_4)_6F_2$. Accordingly, the addition of the highest amount of 0.5 M NH_4F was not enough to form stoichiometric FAp, part of the F^- anions participating in the formation of CaF_2 (Figure 1c).

Inspection of the atomic percent compositions of samples prepared under ATM(37ºC)-conditions, which are included in Table 1, reveals that the incorporation of F^- ions is also lower than the stoichiometric value. However, these samples present a remarkable composition differences with respect to the samples obtained under N_2(37ºC)-conditions. This is reflected by the carbon content and the O/Ca ratio that grow rapidly with x in samples prepared under ATM(37ºC)-conditions while they maintain approximately constant in samples obtained under N_2-conditions. These variations are due to the replacement of PO_4^{3-} by CO_3^{2-}, which as observed by FTIR is a phenomenon promoted by the fluoridation in uncontrolled atmospheres.

Figure 2 compares the WAXS patterns of HAp, *x*F-HAp and FAp prepared under HT- and ATM(37 ºC)-conditions. Characterization of the prepared samples by X-ray diffraction is focused on peaks at 32º-34º 2θ, which are characteristics of the (211),

(112), and (300) HAp reflections. As it can be seen, the diffraction patterns of all minerals are similar and exhibit the peaks associated to the reflections characteristic of the $P6_3/m$ hexagonal crystal structure of HAp, independently of the F^- concentration and the experimental condition used for their preparation. However, it is worth nothing that the peaks of the samples prepared under HT-conditions (*i.e.* air atmosphere with high temperature and pressure) are much better defined than those of minerals obtained at 37 ºC under ATM-conditions, indicating that the crystallinity of *x*F-HAp and FAp is largely affected by pressure and temperature. Accordingly, for each fluorination degree, the crystallinity and crystallite size are higher by more than twice for samples obtained at 150 ºC under a pressure of 200 bars than for those produced at 37 ºC under atmospheric pressure (Table 2).

On the other hand, Table 2 indicates that both crystallinity and crystallite size increases with fluoride substitution. Thus, the crystallinity increases from ~45% and ~10% for HAp to ~61% and ~27% for FAp in samples prepared using HT- and ATM(37º)-conditions, respectively. This should be attributed to the formation of F···H–O hydrogen bonds involving the incorporated F^- anions and the remaining OH^- groups. These interactions, which were examined in previous work [35], help to tight these anions at their crystallographic positions.

Figure 3a displays the TGA and DGTA curves of HAp, *x*F-HAp and FAp prepared under HT-conditions. Initially, all samples display a step at around 100 ºC, which has been attributed to the evaporation of residual water (*i.e.* moisture and water superficially adsorbed). This dehydration process appears as a broad and relatively small peak in the first derivative profile. After this, samples are stable up to a temperature of 145-175 ºC, depending on the composition. At this temperature, the minerals experience a drastic weight loss, which corresponds to the highest peak of the DGTA curve. The weight loss

continues progressively until 600 ºC. At the latter temperature, the weight loss increases with fluorination degree, ranging from 18% for HAp to 22% for FAp. The decomposition peak centered at around 200 ºC has been attributed to the dehydration of the HPO_4^{2-} groups [36], which occur according to the following reaction:

$$2\,HPO_4^{2-} \rightarrow P_2O_7^{4-} + H_2O \qquad (1)$$

At a higher temperature, the progressive variation of the weight has been associated to the loss of CO_2 [36-38]. More specifically, residual type-A CO_3^{2-} can react with HPO_4^{2-} as follows:

$$CO_3^{2-} + HPO_4^{2-} \rightarrow CO_2 + 2\,PO_4^{3-} + H_2O \qquad (2)$$

Above 470 ºC, the weight loss has been associated to the CO_3^{2-} from the lattice (B-type substitution), which undergoes the following reaction [36-38]:

$$CO_3^{2-} + P_2O_7^{4-} \rightarrow 2\,PO_4^{3-} + CO_2 \qquad (3)$$

It is worth noting that the carbonation degree increases with the F^- content, which is also consistent with the weight loss.

The wettability of HAp, *x*F-HAp and FAp prepared under HT- and ATM(37ºC)-conditions was evaluated using water and FBS, the latter mimicking a physiological environment rich in proteins. Results indicate that the contact angles determined for both solvents increases with the fluorination degree (Figures 3b-c), evidencing that the wettability decreases with increasing fluorine content. Moreover, such increment is linear, as is illustrated in Figure S2, which indicates the systematic pattern associated with the substitution of OH^- by F^-. Besides, the contact angle is lower for the sample prepared under HT-conditions than for the one obtained under ATM(37ºC)-conditions, independently of the fluorine content and the solvent. This behavior indicates that, for a

given fluorination degree, the affinity of the mineral surface towards the solvent increases with the crystallinity and the size of the crystals.

As it was expected from results displayed in Figure 3b, the water absorption capacity of the minerals decreases with increasing fluorination degree (Figure 3d), independently of the synthetic conditions. However, it is worth noting that water absorption increases with the crystallinity and crystalline size. Minerals prepared using HT-conditions display a water absorption capacity that is around twice that of minerals prepared using ATM(37ºC)-conditions.

Electrochemical behavior as a function of the fluorination degree

In recent studies the preparation and properties of polarized HAp, hereafter p-HAp, were reported. This electrochemically active material was obtained using a thermally stimulated polarization (TSP) process according to which a constant DC voltage was applied at 1000 ºC for 1 hour to already sintered HAp (s-HAp) [39-40]. The most distinctive characteristic of p-HAp is the electrochemical activity, which is significantly higher than that achieved using lower polarization temperatures to samples sintered in a saturated water atmosphere [41,42]. In a very recent work, an electrophotocatalyst based on p-HAp particles was used to obtain both glycine and alanine (D/L racemic mixture) in mild reaction conditions by fixing nitrogen from N_2 and carbon from CO_2 and CH_4 [40]. Besides, the adsorption of phosphates and phosphonate was found to be significantly higher onto p-HAp than onto as prepared samples [39], where "as prepared samples" refers to unmodified synthesized samples (*i.e.* non-sintered and/or non-polarized minerals).

In this work HAp, *x*F-HAp and FAp powders were sintered at 1000 ºC for 2 hours in air. After this, each sintered sample was processed into discs as described in the

Methods section. Finally, a TSP process was applied to the resulting discs, which were sandwiched between stainless steel (AISI 304) plates and polarized for 1 hour under application of a constant DC voltage at 1000 ºC. After such time, samples were allowed to cool to room temperature, maintaining the DC voltage. Three DC voltages were considered for each sample: 250, 500 and 1000 V.

Polarized samples, hereafter denoted p-HAp, p-*x*F-HAp and p-FAp, were characterized by CV, results being displayed in Figure 4. Cyclic voltammograms recorded in PBS (pH 7.2) for as prepared samples, which were used as controls, reflect a very poor electrochemical behavior (Figure 4a), even though the electrochemical activity was slightly higher than that bare steel (blank) in all cases. In spite of this, the electroactivity of as prepared samples decreases with increasing fluorination degree (*i.e.* the electroactivity is ~63% lower for FAp than for HAp). The electroactivity enhanced considerably after the TSP process, this effect increasing with the applied DC voltage (Figures 4b-d). Again, this increment strongly depends on the fluorination degree. Thus, the electroactivity of p-HAp obtained using 1000 V is ~73% higher than that of as prepared HAp, while the increment is of only ~47% for p-FAp. The dependence of the increment in the electroactivity of the studied minerals against the fluorination degree is represented in Figure 4e, the electroactivity obtained for p-HAp at 1000 V being taken as the reference (100%) for all systems.

Results displayed in Figure 4 are fully consistent with previous observations on p-HAp, which showed that the electrochemically active sites are due to the de-hydroxylation of the crystals during the sintering and the subsequent re-organization of the vacancies into channels during the TSP [39]. The movement of ions through such channels during oxidation and reduction process depends on the concentration of vacancies, which in turn is related with the composition of the prepared mineral. Thus,

the amount of vacancies decreases with increasing fluorination degree since the sintering-induced de-fluorination is much more difficult than the de-hydroxylation. Overall, these results indicate that *x*F-HAp and, especially, FAp are less affected by thermal and electrical treatments than HAp. This stability precludes the use of p-*x*F-HAp and p-FAp in practical applications in which electrochemical properties play a key role, while p-HAp can be used not only as electro-responsive scaffold [39] but also as electrocatalyst to fix nitrogen from N_2 and carbon from CO_2 and CH_4 [40].

Effect of the fluorination degree in the solubility

The remarkable effect of CO_3^{2-} in the solubility of HAp was deeply studied by Pan and Darwell [43]. These authors attributed the increment in the HAp solubility at low pH with the substitution degree by CO_3^{2-} and the formation of complexes such as $CaH_2PO_4H_2CO_3^+$ and $CaH_2PO_4HCO_3$. In order to analyze the effect of CO_3^{2-}-substitution in the solubility of *x*F-HAp and FAp, we firstly prepared different HAp samples by varying the content of CO_3^{2-}. These carbonated HAp samples were obtained using the CO_2-conditions described in the Methods section, the CO_2 atmosphere being maintained during 1, 1.5, 2, 2.5 and 3 hours to achieve different carbonation degrees. The concentration of CO_3^{2-} (in % wt.) in the resulting samples, which was determined by considering that all atomic percent C found by XPS corresponds to such specie (Table 3), increased with the time that the CO_2 atmosphere is applied, ranging from 2.12% (1 hour) to 16.30% (3 hours).

The solubility of the carbonated HAp was evaluated by adding 500 mg of each sample to an aqueous solution (50 mL) with 100 mM HCl and 50 mM NaCl. Figure 5a shows that, as it was expected, the solubility of HAp increases rapidly with the

carbonation degree (*i.e.* from ~78 to ~763 mM when the carbonation time increased from 1 to 3 h; Table 3). In contrast, the solubility in the same medium decreases significantly with the fluorination degree, as is evidence in Figure 5b for HAp, *x*F-HAp and FAp samples prepared under controlled N_2(37ºC)-conditions. Thus, the content of CO_3^{2-} in these samples was very low, as was discussed above (Table 1).

A completely different behavior was obtained for *x*F-HAp and FAp prepared using ATM(37ºC)-conditions (Figure 5c). In this case, the content of CO_3^{2-} increases with the fluorination degree, ranging from 2.67% wt. (0.4F-HAp) to 16.03% wt. (FAp), as is explicitly labelled in Figure 5c, and, therefore, the solubility in the acid medium increases considerably with the fluorination degree. However, such solubility is still significantly lower than that of HAp prepared under CO_2-conditions (Figure 5a), even though the carbonation degree was similar in both cases. Thus, the inhibitory effect associated for the F^- anions and the unrestrictive effect attributed to the CO_3^{2-} anions coexist in *x*F-HAp and FAp samples prepared using ATM(37ºC)-conditions.

In order to examine the effect of external F^- anions in the solubility of HAp prepared under N_2(37ºC)- and CO_2-conditions (CO_2 atmosphere maintained for 1 hour), very small F^- concentrations were supplied by adding NH_4F to the acid solubility medium. The variation of the solubility of these minerals as a function of the supplied F^- concentration, [F^-], is compared in Figure 5d. As it was expected, both cases, the solubility decreases with increasing external [F^-]. This general behavior was independent of the presence of CO_3^{2-} in the mineral matrix, even though samples prepared CO_2-conditions, which contain 2.12% wt. CO_3^{2-}, exhibited higher solubility for all the explored [F^-] concentrations. Similar observations were obtained for 0.8F-

HAp prepared under N_2(37ºC)- and CO_2-conditions (CO_2 atmosphere maintained for 1 hour), as is reflected in Figure 5e.

Overall, comparison of results displayed in Figure 5 indicates that, although the incorporation of F^- into the mineral matrix reduces the solubility, external F^- anions surrounding the HAp matrix inhibit such process more effectively. Probably, the latter anions are partially adsorbed onto the mineral surface and a dynamical equilibrium with the solution, which involves re-precipitation processes, is reached. These results have remarkable implications for the use of HAp as mineral coating for dental implants. Thus, implants made from titanium, stainless steel or cobalt-chrome alloys are frequently modified at the surface by bioceramics coatings that can be applied using different technologies, even though plasma spraying is the most popular and the Food and Drug Administration (FDA)-approved method [44]. In recent years, strategies based on the substitution of HAp by *x*F-HAp or FAp coatings has been proposed as effective strategies to decrease biofilm accumulation, to inhibit the demineralization process and to combat caries-related bacteria [45-49]. However, our results clearly indicate that such fluoride-therapy is more effective by supplying F^- anions to the HAp coating from an external source (e.g. frequent mouthwashes with a fluoride solution) than incorporating such anions into the own mineral matrix replacing HAp by *x*F-HAp or FAp.

On the other hand, it is well known that the solubility of some minerals, as for example NaCl, is practically independent of the pH, while the solubility of HAp increases approximately 10 times for each unit of decrease in pH. Similar pH dependence has been reported for FAp [43], which was reported to exhibit a solubility profile just below and nearly parallel to that of HAp. Figure S3, which represents the solubility of *x*F-HAp against the change of pH within the $2.0 \leq pH \leq 3.0$ interval, proves that such behavior is independent of the fluorination degree. These experiments, in

which mimic the bacterial acid attack, support previous discussion, indicating that fabrication of HAp mineral coatings with a low or null fluorination degree is the most appropriated.

CONCLUSIONS

Synthetic HAp, *x*F-HAp and FAp have been prepared using experimental conditions that differ in the environment, the temperature and/or the pressure. The synthetic conditions regulate the mineral composition in terms of CO_3^{2-} and F^- intake, the formation of vacancies, the water absorption, the crystallinity, and crystallite size. The solubility in aqueous acid media of the prepared minerals depends on their composition. More specifically, the solubility increases with the CO_3^{2-} content while it decreases with increasing fluorination degree. Moreover, the inhibitory effect associated to the F^- anions contained in the mineral matrix of *x*F-HAp and FAp enhances when F^- anions are supplied to HAp through an external solution. These results have important implications that affect the mineral coatings used to protect dental implants. Thus, non-carbonated HAp coatings enriched in F^- anions through external sources are more suitable for inhibiting demineralization than the recently proposed *x*F-HAp and FAp coatings, which contain the F^- anions within the mineral matrix.

ACKNOWLEDGEMENTS

This work was supported by B. Braun Surgical S.A. through a joint research agreement with UPC, and by the MINECO/FEDER (MAT2015-69367-R and MAT2015-69547-R) and the Agència de Gestió d'Ajuts Universitaris i de Recerca (2017SGR359). Support for the research of C.A. was received through the prize "ICREA Academia" for excellence in research funded by the Generalitat de Catalunya.

This work is integrated within a wider research project supported by B. Braun Surgical S.A., UPC and ICFO and H. Germans Trias i Pujol.

REFERENCES

[1] H. W. Kim, H. E. Kim, J. C. Knowles, Fluor-hydroxyapatite sol-gel coating on titanium substrate for hard tissue implants, *Biomaterials*, 2004, **25**, 3351-3358.

[2] R. Ebrahimi-kahrizsangi, B. Nasiri-Tabrizi, A. Chami, Synthesis and characterization of fluorapatite-titania (FAp-TiO_2) nanocomposite via mechanochemical process, *Solid. State. Sci*., 2010, **12**, 1645-1651.

[3] K. Tosuaaddu, K. A. Gross, L. Pluduma, M. Veiderma, A review on the thermal stability of calcium apatites, *J. Therm. Anal. Calorim.*, 2012, **110**, 647-659.

[4] L. Rintoul, E. Wentrup-Byrne, S. Suzuki, L. Grøndahl, FT-IR spectroscopy of fluoro-substituted hydroxyapatite: strengths and limitations, *J. Mater. Sci. Mater. Med.*, 2007, **18**, 1701–1709.

[5] C. Wang, G. A. Karlis, G. I. Anderson, C. R. Dunstan, A. Carbone, G. Berger, U. Ploska, H. Zreidat, Bone growth is enhanced by novel bioceramic coatings on Ti alloy implants, *J. Biomed. Mater. Res., Part A.*, 2009, **90A**, 419-428.

[6] H. B. Qu, M. Wei, The effect of fluoride contents in fluoridated hydroxyapatite on osteoblast behavior, *Acta Biomater.*, 2006, **2**, 113-119.

[7] I. Heling, R. Heindel, B. Merin, Calcium-fluorapatite. A new material for bone implants, *J. Oral Implantol.*, 1981, **9**, 548-555.

[8] S. V. Dorozhkin, Calcium orthophosphates. Occurrence, properties, biomineralization, pathological calcification and biomimetic applications, *Biomatter.*, 2011, **1**, 121-164.

[9] M. A. S. Melo, S. F. F. Guedes, H. H. K. Xu, L. K. A. Rodrigues, Nanotechnology-based restorative materials for dental caries management, *Trends Biotechnol.*, 2013, 31, 459-467.

[10] A. Moshaverinia, S. Ansari, M. Moshaverinia, N. Roohpour, J. A. Darr, I. Rehman, Effects of incorporation of hydroxyapatite and fluoroapatite nanobioceramics into conventional glass ionomer cements (GIC), *Acta Biomater.*, 2008, **4**, 432-440.

[11] A. Saber, A. Smahi, A. Solhy, R. Nazih, B. Elaabar, M- Maizi, S. Sebti, Heterogeneous catalysis of Friedel-Crafts alkylation by the fluorapatite alone and doped with metal halides, *J. Mol. Catal. A: Chem.*, 2003, **202**, 229-237.

[12] Z. Boukha, M. Kacimi, M. Ziyad, A. Ensuque, F. Bozon-Verduraz, Comparative study of catalytic activity of Pd loaded hydroxyapatite and fluoroapatite in butan-2-ol conversion and methane oxidation, *J. Mol. Catal. A Chem.*, 2007, **270**, 205-213.

[13] H. Li, L. Mei, H. Liu, Y. Liu, L. Liao, R. V. Kumar. Growth mechanism of surfactant-free size-controlled luminescent hydroxyapatite nanocrystallites, *Cryst. Growth Des.*, 2017, **17**, 2809-2815.

[14] Q. H. Yuan, A. P. Xu, Z. Q. Zhang, Z. H. Chen, L. Wan, X. Shi, S. X. Lin, Z. Y. Yuan, L. B. Deng. Bioactive silver doped hydroxyapatite composite coatings on metal substrates: Synthesis and characterization, *Mat. Chem. Phys.*, 2018, **218**, 130-139.

[15] A. C. Popescu, P. E. Florian, G. E. Stan, G. Popescu-Pelin, J. Zgura, M. Enculescu, F. N. Oktar, R. Trusca, L. E. Sima, A. Roseanu, L. Duta.Physical-chemical characterization and biological assessment of simple and lithium-doped biological-derived hydroxyapatite thin films for a new generation of metallic implants. *Appl. Surf. Sci.*, 2018, **439**, 724-735.

[16] A. Z. Alshemary, A. E. Pazarceviren, A. Tezcaner, Z. Evis. Fe^{3+}/SeO_4^{2-} dual doped nano hydroxyapatite: A novel material for biomedical applications, *J. Biomed. Mater. Res. B*, 2018, **106**, 340-352.

[17] Y. Xu, L. An, L. L. Chen, L. Cao, D. L. Zeng, G. H. Wang, A Facile chemical route to synthesize Zn doped hydroxyapatite nanorods for protein drug delivery, *Mater. Chem. Phys.*, 2018, **214**, 359-363.

[18] K. A. Bhadang, C. A. Holding, H. Thissen, K. M. McLean, J. S. Forsythe, D. R. Haynes, Biological responses of human osteoblasts and osteoclasts to flame-sprayed coatings of hydroxyapatite and fluorapatite blends, *Acta Biomater.*, 2010, **6**, 1575-1583.

[19] H. Ye, X. Y. Liu, H. P. Hong, Cladding of titanium/fluorapatite composites onto Ti6Al4V substrate and the *in vitro* behaviour in the simulated body fluid, *Appl. Surf. Sci.*, 2009, **255**, 8126-8134.

[20] F. Müller, C. Zeith, H. Mantz, K.-H. Ehses, F. Soldera, J. Schmauch, M. Hanning, Elemental depth profiling of fluoridated hydroxyapatite: Saving your dentition by the skin of your teeth?, *Langmuir*, 2010, **26**, 18750-18759.

[21] N. Jmal, J. Bouaziz, Synthesis, characterization and bioactivity of a calcium-phosphate glass-ceramics obtained by the sol-gel processing method, *Mater. Sci. Eng. C*, 2017, **71**, 279-288.

[22] Z. P. Li, B. X. Huang, S. Mai, X. Y. Wu, H. Q. Zhang, W. Qiao, X. Luo, Z. F. Chen, Effects of fluoridation of porcine hydroxyapatite on osteoblastic activity of human MG63 cells, *Sci. Technol. Adv. Mater.*, 2015, **16**, 035006.

[23] V. Stanic, S. Dimitrijevic, D. G. Antonovic, B. M. Jokic, S. P. Zec, S. T. Tanaskovic, S. Raicevic, Synthesis of fluorine substituted hydroxyapatite nanopowders and application of the central composite design for determination of its antimicrobial effects, *Appl. Surf. Sci.*, 2014, **290**, 346-352.

[24] S. Kannan, S. I. Vieira, S. M. Olhero, P. M. C. Torres, S. Pina, O. Silva, J. M. F. Ferreira, Synthesis, mechanical and biological characterization of ionic doped carbonated hydroxyapatite/*β*-tricalcium phosphate mixtures, *Acta Biomater.*, 2011, **7**, 1835-1843.

[25] P. J. Marie, M. Hott, Short-term effects of fluoride and strontium on bone formation and resorption in the mouse, *Metabolism*, 1986, **35**, 547-551.

[26] R. M. Wilson, J. C. Elliott, S. E. P. Dowker, R. I. Smith, Rietveld structure refinement of precipitated carbonate apatite using neutron diffraction data, *Biomaterials*, 2004, **25**, 2205-2213.

[27] J. A. Cury, S. B. Francisco, G. S. Simoes, A. A. Del Bel Cury, C. P. M. Tabchoury, Effect of a calcium carbonate-based dentifrice on enamel demineralization in situ, *Caries Res.*, 2003, **37**, 194-199.

[28] J. Kolmas, U. Piotrowska, M. Kuras, E. Kurek, Effect of carbonate substitution on physicochemical and biological properties of silver containing hydroxyapatites, *Mater. Sci. Eng. C*, 2017, **74**, 124-130.

[29] K. Igeta, Y. Kuwamura, N. Horiuchi, K. Nozaki, D. Shiraishi, M. Aizawa, K. Hashimoto, K. Yamashita,, A. Nagai, Morphological and functional changes in RAW264 macrophage-like cells in response to a hydrated layer of carbonate-substituted hydroxyapatite, *J. Biomed. Mater. Res. Part A*, 2017, **105**, 1063-1070.

[30] G. S. Kumar, A. Thamizhavel, Y. Yokogawa, S. N. Kalkura, E. K. Girija, Synthesis, characterization and *in vitro* studies of zinc and carbonate co-substituted nano-hydroxyapatite for biomedical applications, *Mater. Chem. Phys*., 2012, **134**, 1127-1135.

[31] L. J. del Valle, O. Bertran, G. Chaves, G. Revilla-López, M. Rivas, M. T. Casas, J. Casanovas, P. Turon, J. Puiggalí, C. Alemán, DNA adsorbed on hydroxyapatite surfaces, *J. Mater. Chem. B*, 2014, **2**, 6953-6966.

[32] Q.-X. Zhu, Y.-M. Li, D. Han, Co-substitution of carbonate and fluoride in hydroxyapatite: Effect on substitution type and content, *Front. Mater. Sci.*, 2015, **9**, 192-198.

[33] Y. Wang, S. Zhang, X. Zeng, L. L. Ma, W. Weng, W. Ya, M Qian, Osteoblastic cell response on fluoridated hydroxyapatite coatings, *Acta Biomater.*, 2007, **3**, 191-197.

[34] K. Cheng, S. Zhang, W. J. Weng, Comparison of microstructure and chemical composition of hydroxyapatite and fluorapatite coatings deposited on Ti-6Al-4V substrates by Nd-YAG laser, *Surf. Coat. Technol.*, 2005, **198**, 237-241.

[35] H. Li, W. Huang, Synthesis of fluorapatite–hydroxyapatite nanoparticles and toxicity investigations, *Mater. Sci. Eng. C*, 2007, **27**, 756-761.

[36] S. Masmoudia, A. Larbot, H. El Feki, R. Ben Amarm, Elaboration and properties of new ceramic microfiltration membranes from natural and synthesised apatite, *Desalination*, 2006, **190**, 89-103.

[37] A. A. Chauhdry, J. C. Knowles, I. Rehman, J. A. Darr, Rapid hydrothermal flow synthesis and characterisation of carbonate- and silicate-substituted calcium phosphates, *J. Biomater. Appl.*, 2013, **28**, 448-461.

[38] N. A.M. Barakat, K.A. Khalil, F. A. Sheikh, A.M. Omran, B. Gaihre, S. M. Khil, H. Y. Kim, Physiochemical characterizations of hydroxyapatite extracted from bovine bones by three different methods: Extraction of biologically desirable HAp, *Mater. Sci. Eng. C*, 2008, **28**, 1381-1387.

[39] M. Rivas, L. J. del Valle, E. Armelin, O. Bertran, P. Turon, J. Puiggalí and C. Alemán, Hydroxyapatite with permanent electrical polarization: Preparation,

characterization, and response against inorganic adsorbates, *Chem. Phys. Chem.*, 2018, **19**, 1746-1753.

[40] M. Rivas, L. J. del Valle, P. Turon, C. Alemán, J. Puiggalí, Sustainable synthesis of amino acids by catalytic fixation of molecular dinitrogen and carbon dioxide, *Green Chem.*, 2018, **20**, 685-693.

[41] M. Nakamura, Y. Sekijima, S. Nakamura, T. Kobayashi, K. Niwa, K. Yamashita, Role of blood coagulation components as intermediators of high osteoconductivity of electrically polarized hydroxyapatite, *J. Biomed. Mater. Res.*, 2006, **79A**, 627-634.

[42] N. Horiuchi, S. Nakaguki, N. Wada, M. Nakamura, A. Nagai, K. Katayama, K. Yamashita, Polarization-induced surface charges in hydroxyapatite ceramics, *J. Appl. Phys.*, 2014, **116**, 014902.

[43] H. B. Pan, B. W. Darvell, Solubility of TTCP and β-TCP by solid tritation. *Arch. Oral Biol.*, 2009, **54**, 671-677.

[44] A. A. Campbell, Bioceramics for implant coatings, *Mater. Today*, 2003, **6**, 26-30.

[45] M. A. S. Melo, S. F. F. Guedes, H. H. K. Xu, L. K. A. Rodrigues, Nanotechnology-based restorative materials for dental caries management, *Trends Biotechnol.*, 2013, **31**, 459-467.

[46] A. Moshaverinia, S. Ansari, Z. Movasaghi, R. W. Billington, J. A. Darr, I. U. Rehman, Modification of conventional glass-ionomer cements with N-vinylpyrrolidone containing polyacids, nano-hydroxy and fluoroapatite to improve mechanical properties, *Dent Mater.*, 2008, **24**, 1381-1390.

[47] E. Pepla, L. K. Besharat, G. Palaia, G. Tenore, G. Migliau, Nano-hydroxyapatite and its applications in preventive, restorative and regenerative dentistry: a review of literature, *Ann. Stomatol.*, 2014, **5**, 108-114.

[48] A. Alhilou, T. Do, L. Mizban, B. H. Clarkson, D. J. Wood and M. G. Katsikogianni, Physicochemical and antibacterial characterization of a novel fluorapatite coating, *ACS Omega*, 2016, **1**, 264-276.

[49] X. Ge, Y. Leng, C. Bao, S. L. Xu, R. Wang, F. Ren, Antibacterial coatings of fluoridated hydroxyapatite for percutaneous implants, *J. Biomed. Mater. Res. Part A*, 2010, **95**, 588-599.

Table 1. Atomic percent composition (Ca, P, O, F and C) of HAp, *x*F-HAp and FAp prepared under N_2(37ºC)- and ATM(37ºC)-conditions. Ca/P, F/Ca and O/Ca ratios are displayed for each compound.

	Ca	**P**	**O**	**F**	**C**	**Ca/P**	**F/Ca**	**O/Ca**
				N_2(37º)-conditions				
HAp	39.69	19.18	40.94	0.0001	0.19	1.60	0.002	2.57
0.4F-HAp	39.82	19.15	40.80	0.0023	0.23	1.61	0.044	2.55
0.8F-HAp	39.81	18.91	41.11	0.0037	0.17	1.63	0.071	2.58
1.2F-HAp	39.77	18.58	41.44	0.0065	0.21	1.65	0.124	2.60
1.6F-HAp	39.72	18.47	41.65	0.0086	0.15	1.66	0.165	2.62
FAp	40.00	18.48	41.42	0.0100	0.09	1.67	0.190	2.58
				ATM(37ºC)-conditions				
HAp	38.29	18.18	43.34	0.0001	0.19	1.63	0.002	2.83
0.4F-HAp	35.80	16.87	46.82	0.0020	0.51	1.64	0.043	3.27
0.8F-HAp	33.87	15.95	49.25	0.0035	0.93	1.64	0.079	3.63
1.2F-HAp	29.77	14.01	54.81	0.0046	1.41	1.64	0.118	4.60
1.6F-HAp	26.72	12.47	58.91	0.0055	1.89	1.66	0.157	5.51
FAp	25.42	12.01	60.49	0.0064	2.08	1.64	0.195	5.95

Table 2. Crystallinity (χ_c) and crystallite size (L) of HAp, *x*F-HAp and FAp prepared under HT- and ATM(37ºC)-conditions.

	HT-conditions		**ATM(37ºC)-conditions**	
	χ_c (%)	L (nm)	χ_c (%)	L (nm)
HAp	44.7±1.0	49.8±1.4	9.7±1.7	10.3±0.5
0.4F-HAp	47.2±1.3	55.6±1.0	13.4±1.1	13.1±0.8
0.8F-HAp	50.7±1.4	60.6±1.9	16.3±0.7	17.3±1.8
1.2F-HAp	53.7±1.6	66.1±2.1	19.4±1.8	22.4±1.4
1.6F-HAp	57.9±1.5	70.8±2.6	22.3±1.9	27.0±1.7
FAp	61.1±1.0	76.2±1.7	26.7±1.2	32.5±1.4

Table 3. Atomic percent composition (Ca, P, O, F and C), Ca/P ratio and content of CO_3^{2-} (in % wt.) as determined by XPS of HAp prepared using ATM- and CO_2-conditions. For the latter, the CO_2 atmosphere was during a time comprised between 1 and 3 hours (indicated in parenthesis). The % wt. of CO_3^{2-} was determined assuming that all atomic percent content of C corresponds to CO_3^{2-}. The solubility in an aqueous solution with 100 mM HCl and 50 mM NaCl is also displayed.

Conditions	**Ca**	**P**	**O**	**C**	**F**	**Ca/P**	**% CO_3^{2-}**	**Solubility (mM)**
ATM	38.78	18.12	42.96	0.14	0.0003	1.65	0.27	19.5±0.6
CO_2 (1 h)	36.50	16.84	46.34	0.32	0.0002	1.67	2.12	77.6±2.8
CO_2 (1.5 h)	34.36	15.80	49.28	0.56	0.0002	1.68	5.10	215.0±5.2
CO_2 (2 h)	30.12	14.01	54.98	0.89	0.0003	1.66	8.50	468.7±6.9
CO_2 (2.5 h)	26.85	12.32	59.38	1.45	0.0002	1.68	11.67	694.1±10.2
CO_2 (3.0 h)	24.12	11.15	62.95	1.78	0.0003	1.67	16.30	763.5±14.3

CAPTIONS TO FIGURES

Figure 1. FTIR spectra of HAp, *x*F-HAp and FAp samples prepared using (a) ATM(37ºC)- and (b) N_2(37ºC)-conditions. The position of the main bands for CO_3^{2-} and water are displayed using red and blue dashed lines, respectively. (c) High-resolution XPS spectra in the F 1s region for HAp, *x*F-HAp and FAp samples prepared using N_2(37ºC)-conditions.

Figure 2. X-ray diffraction patterns of HAp, *x*F-HAp and FAp samples prepared under HT-conditions at 150 ºC and ATM(37ºC)-conditions. The hexagonal structure typically observed for HAp was identified by the peaks associated to the (211), (112) and (300) reflections.

Figure 3. (a) TGA (left) and DTGA (right) curves for HAp, *x*F-HAp and FAp samples prepared under HT-conditions. Contact angles of (b) water and (c) FBS, and (d) water absorption capacity for HAp, *x*F-HAp and FAp samples prepared under HT- and ATM(37ºC)-conditions.

Figure 4. Control voltammograms of HAp, *x*F-HAp and FAp: (a) as prepared and polarized through a TSP process using a DC voltage of (b) 250 V, (c) 500 V and (d) 1000 V. Voltammograms for bare steel (blank) are included in all cases. (e) Variation of the electrochemical activity with the polarization process using different DC voltages. Values are relative to p-HAp obtained using 1000 V (taken as 100%).

Figure 5. Solubility in aqueous solution with 100 mM HCl and 50 mM NaCl against: (a) the % of CO_3^{2-} (in wt.) of HAp prepared using CO_2-conditions (37 ºC), which were applied during different times to achieve different carbonation degrees; (b) the fluorination degree (expressed as F/Ca ratio) of HAp, *x*F-HAp and FAp prepared under N_2(37ºC)-conditions ; (c) the fluorination degree (expressed as F/Ca ratio) of HAp, *x*F-HAp and FAp prepared under ATM(37º)-conditions Numerical labels indicate the % of

CO_3^{2-} (in wt.) in the prepared samples as determined by XPS; (d) the [F^-] supplied to the solubility medium of HAp prepared using N_2(37ºC) and CO_2-conditions. In the latter, the CO_2 atmosphere was applied during 1 hour; and (e) the [F^-] supplied to the solubility medium of 0.8F-HAp prepared using N_2(37ºC)- and CO_2-conditions. In the latter, the CO_2 atmosphere was applied during 1 hour.

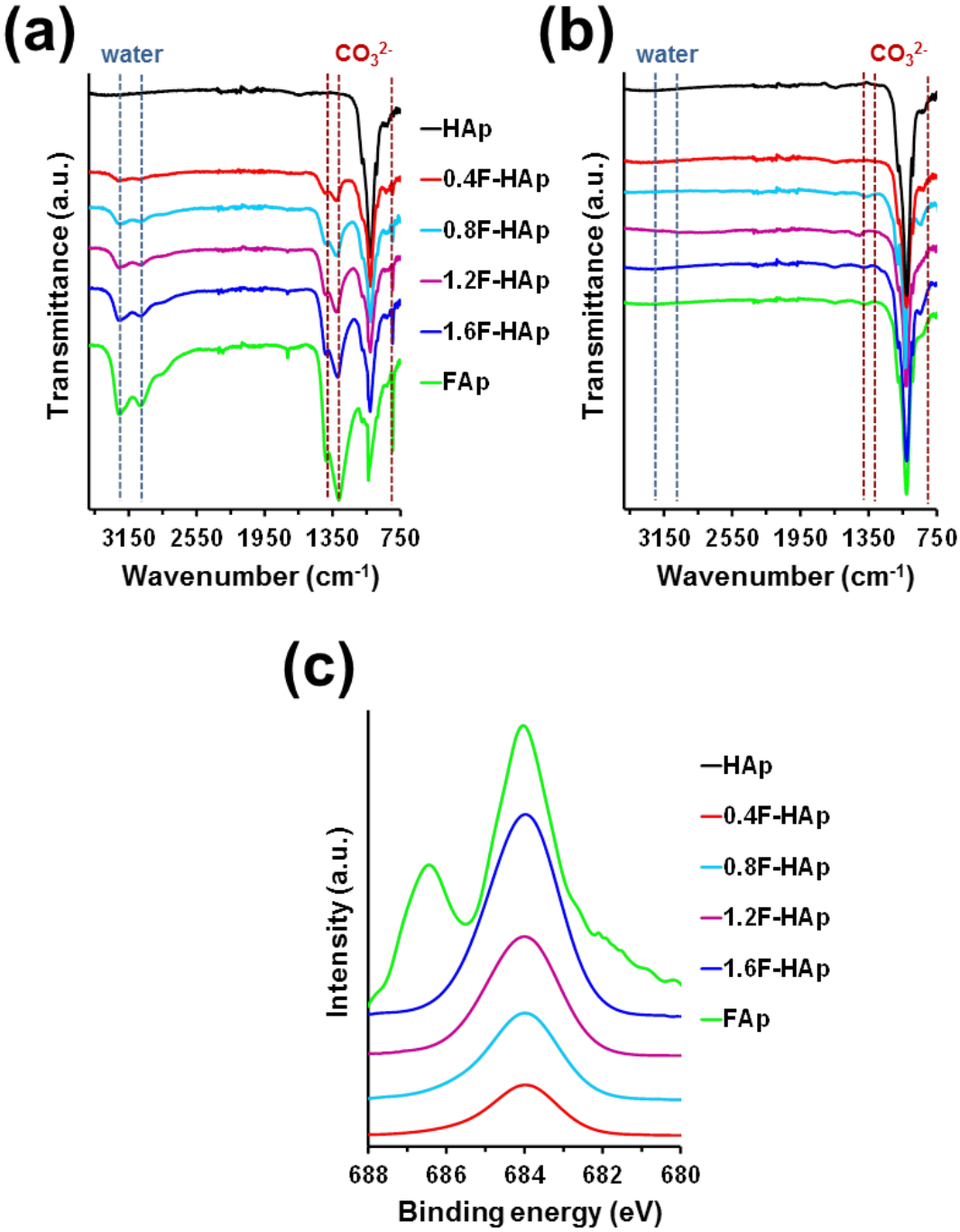
(a)
water
CO_3^{2-}
Transmittance (a.u.)
3150 2550 1950 1350 750
Wavenumber (cm^{-1})
HAp
0.4F-HAp
0.8F-HAp
1.2F-HAp
1.6F-HAp
FAp
(b)
water
CO_3^{2-}
Transmittance (a.u.)
3150 2550 1950 1350 750
Wavenumber (cm^{-1})
(c)
Intensity (a.u.)
688 686 684 682 680
Binding energy (eV)
HAp
0.4F-HAp
0.8F-HAp
1.2F-HAp
1.6F-HAp
FAp

Figure 1

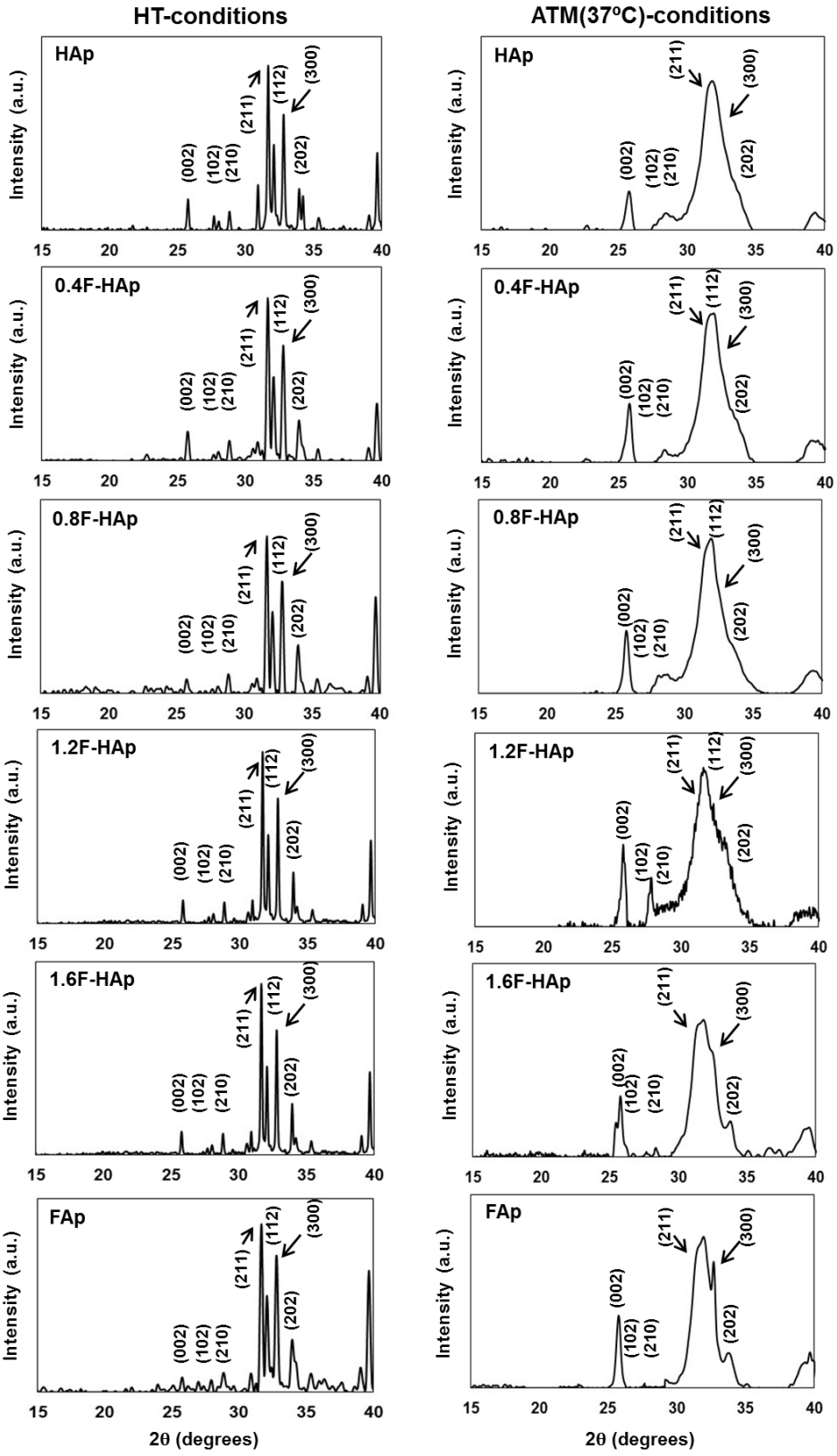
HT-conditions
ATM(37ºC)-conditions
HAp
0.4F-HAp
0.8F-HAp
1.2F-HAp
1.6F-HAp
FAp
Intensity (a.u.)
2θ (degrees)
(002)
(102)
(210)
(211)
(112)
(202)
(300)
15
20
25
30
35
40

Figure 2

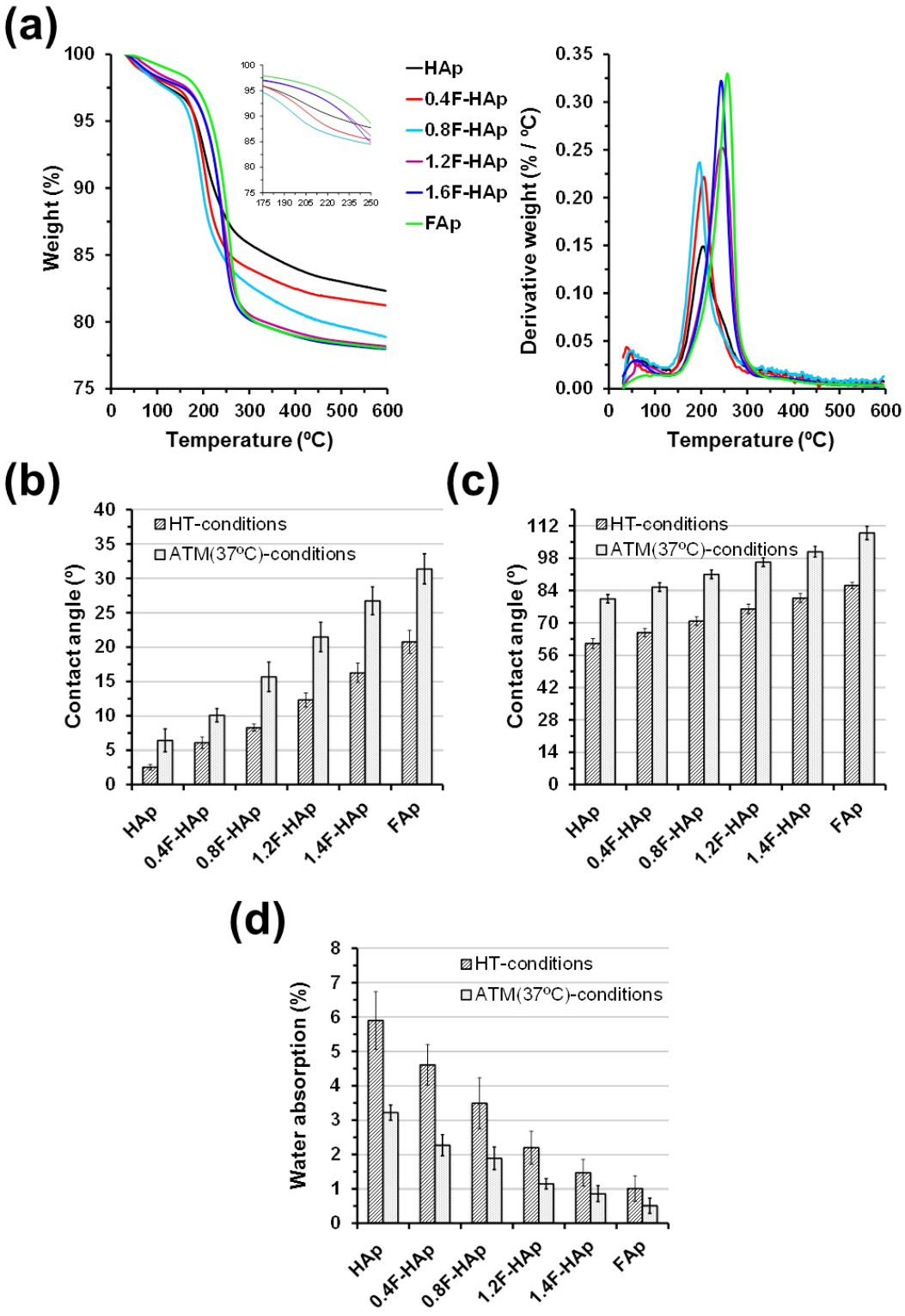
(a)
Weight (%)
Temperature (ºC)
HAp
0.4F-HAp
0.8F-HAp
1.2F-HAp
1.6F-HAp
FAp
Derivative weight (% / ºC)
Temperature (ºC)
(b)
Contact angle (º)
HT-conditions
ATM(37ºC)-conditions
HAp
0.4F-HAp
0.8F-HAp
1.2F-HAp
1.4F-HAp
FAp
(c)
Contact angle (º)
HT-conditions
ATM(37ºC)-conditions
HAp
0.4F-HAp
0.8F-HAp
1.2F-HAp
1.4F-HAp
FAp
(d)
Water absorption (%)
HT-conditions
ATM(37ºC)-conditions
HAp
0.4F-HAp
0.8F-HAp
1.2F-HAp
1.4F-HAp
FAp

Figure 3

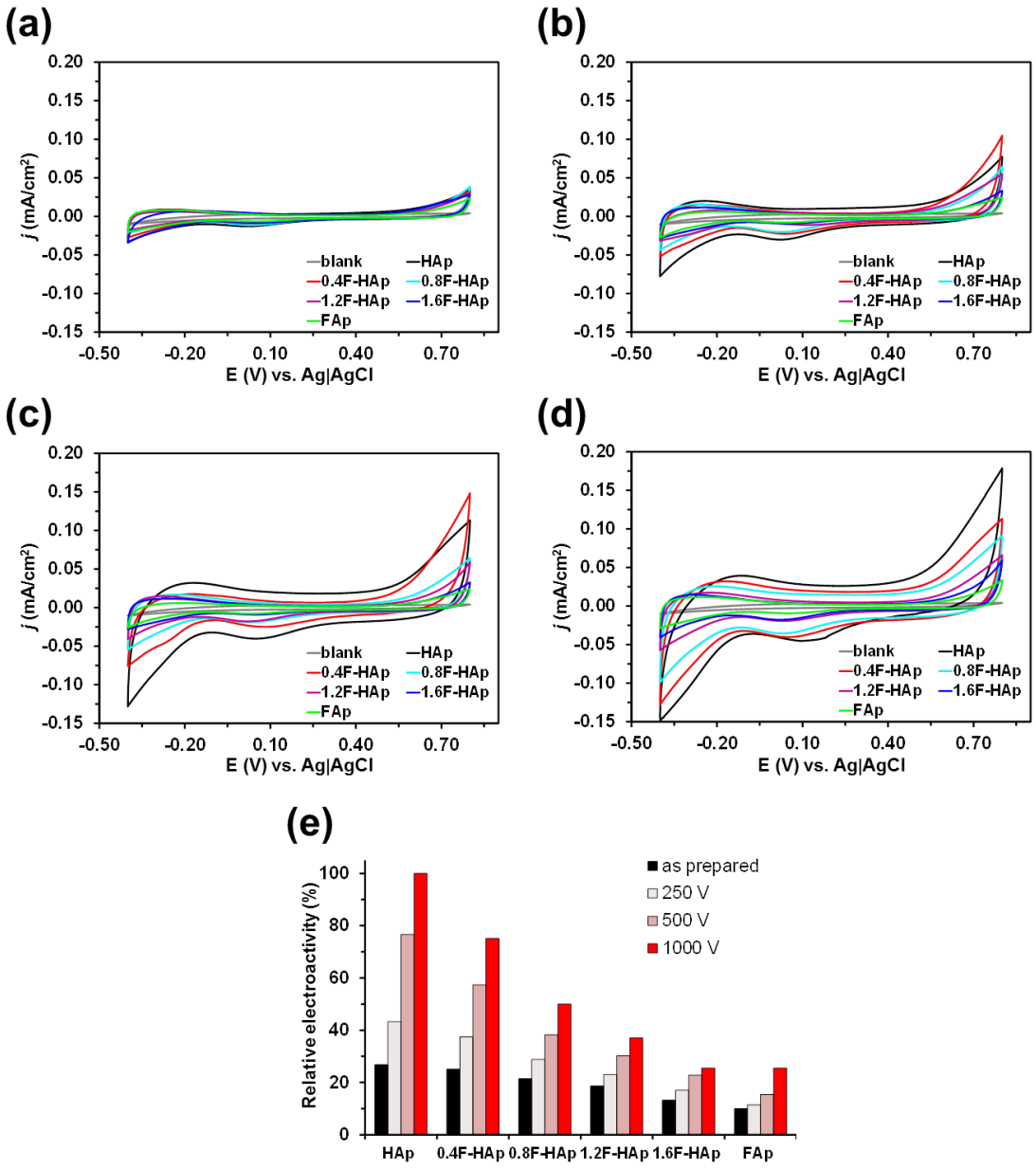
(a)
(b)
(c)
(d)
(e)
j (mA/cm²)
E (V) vs. Ag|AgCl
blank
HAp
0.4F-HAp
0.8F-HAp
1.2F-HAp
1.6F-HAp
FAp
Relative electroactivity (%)
as prepared
250 V
500 V
1000 V
HAp
0.4F-HAp
0.8F-HAp
1.2F-HAp
1.6F-HAp
FAp

Figure 4

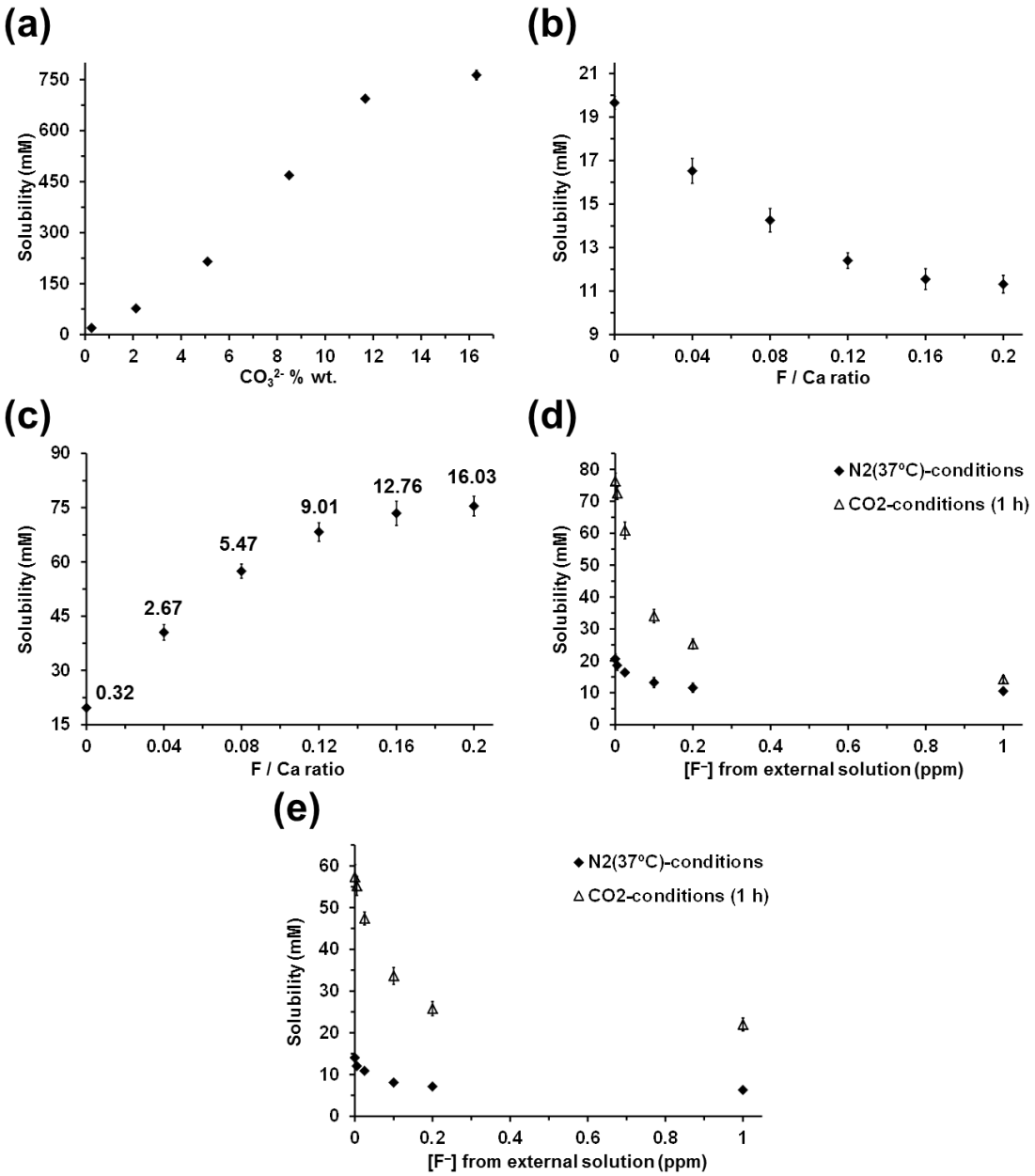
(a)
Solubility (mM)
CO_3^{2-} % wt.
(b)
Solubility (mM)
F / Ca ratio
(c)
Solubility (mM)
0.32
2.67
5.47
9.01
12.76
16.03
F / Ca ratio
(d)
Solubility (mM)
N2(37°C)-conditions
CO2-conditions (1 h)
[F⁻] from external solution (ppm)
(e)
Solubility (mM)
N2(37°C)-conditions
CO2-conditions (1 h)
[F⁻] from external solution (ppm)

Figure 5

GRAPHICAL ABSTRACT